



# Vacuum and Hover Tests of a Dihedral–Anhedral Tip Composite Rotor

Cheng Chi\*<sup>✉</sup> and Anubhav Datta<sup>†</sup>

*University of Maryland, College Park, Maryland 20740*

and

Brahmananda Panda<sup>‡</sup>

*The Boeing Company, Ridley Park, Pennsylvania 19078*

<https://doi.org/10.2514/1.C037321>

**This paper presents test data from vacuum and hover tests of a 2.8-ft-radius dihedral–anhedral tip composite rotor. The paper describes the blades, their fabrication, properties, instrumentation, the test conditions, and the data acquired. The blades were Mach-scaled to a generic but representative modern rotor. Vacuum chamber tests measured rotating frequencies and strains. Hover tests measured performance, blade loads, pitch-link loads, and strains under steady and cyclic loading conditions. Three-dimensional finite element structural models were developed to ensure completeness and consistency of property definition. The three-dimensional analysis was also used for a preliminary assessment of the test data. The test data revealed that the dihedral–anhedral tip influences the torsional and higher frequencies of a rotor blade significantly. The oscillatory blade loads show patterns consistent with the vertical center-of-gravity offset introduced by the tip. The surface strains reveal interesting higher-harmonic patterns of loading particularly near the dihedral junction.**

## Nomenclature

$A$	=	rotor disk area, $\pi R^2$ , m <sup>2</sup>
$A_b$	=	rotor blade area projected on disk, m <sup>2</sup>
$C_P$	=	power coefficient, rotor power/ $\rho A V_{\text{tip}}^3$
$C_T$	=	thrust coefficient, rotor thrust/ $\rho A V_{\text{tip}}^2$
$C_T/\sigma$	=	blade loading, rotor thrust/ $\rho A_b V_{\text{tip}}^2 \sigma$
$E$	=	Young's modulus, GPa
$G$	=	shear modulus, GPa
$M_{\text{tip}}$	=	tip Mach number
$R$	=	rotor radius, m
$V_{\text{tip}}$	=	tip speed, $\Omega R$ , m/s
$\gamma_{xy}$	=	engineering shear strain
$\epsilon_{xx}$	=	axial normal strain
$\epsilon_{yy}$	=	chordwise normal strain
$\theta_{1C}$	=	lateral cyclic, deg
$\theta_{75}$	=	collective pitch at 75% radius, deg
$\nu$	=	Poisson's ratio
$\rho$	=	air density, kg/m <sup>3</sup>
$\sigma$	=	rotor solidity, blade area/ $\pi R^2$
$\Omega$	=	rotational speed, rad/s

## I. Introduction

**T**HE objective of this work is to measure the hover performance, rotor frequencies, strains, and structural loads of a 0.853-m (2.8-ft)-radius Mach-scaled helicopter rotor with a dihedral–anhedral tip. The measurements are meant to provide basic understanding of the aeromechanics of these tips and validation data for advanced analysis software.

Anhedral tips are ubiquitous in modern airplanes but are less common in helicopter rotors. The helicopter rotor is the principal source of lift, propulsion, and control—all combined—and due to their slender and flexible nature the blade tips, which encounter the

highest dynamic pressure, three-dimensional (3-D) transonic flow, intense  $g$  levels, and maximum deformations, play a very sensitive role in the design of the aircraft. The slightest shift in center of gravity (c.g.) near the tip introduces complex inertial and aerodynamic couplings that can have an enormous impact on blade and pitch-link loads. For decades, rotorcraft engineers and researchers have tried various tip geometries to design better rotor blades—blades that alleviate loads, vibration, and noise while enhancing performance. Today, several types of advanced tip geometries can be found on helicopters, for example, the swept-tip on Sikorsky UH-60, double swept-tip on Airbus H160, swept-tip with forward offset (paddle tip) on the Augusta Westland Merlin Mk3, the anhedral tip on Sikorsky S-92, and the more recent dihedral–anhedral tip on Boeing CH-47. Among these, the dihedral–anhedral tip has been studied the least.

Anhedral tips rotate the cross sections down away from the plane of rotation. Like on an airplane wing, an anhedral tip can improve performance, particularly hover performance of a helicopter. It can also change the position of the tip vortex and its interaction with the following blade influencing vibration and noise. But these benefits come at the price of a c.g. offset near the tip. The intent of a special construction that has a dihedral first followed by an anhedral is to bring the net c.g. effectively back near the rotor plane. Recently, such attempts on a full-scale rotor have shown improved hover but excessive loads. The intent of this paper is to fabricate and test such a rotor. But first, the history of anhedral tips is briefly reviewed, with emphasis on testing.

### A. Anhedral Tip in Airplane Wings

There is a vast literature on anhedral wing tips. The concept of what can generally be called a nonplanar end plate or winglet to improve wing performance can be traced back to a British patent by Frederick Lanchester in 1898 [1] long before airplanes were invented. Lanchester called them “planes” arranged normally to the wing surfaces and conformably to the direction of flight. Later, after the invention of airplanes, between 1920s to 1950s, the work of Reid [2], Hemke [3], Mangler [4], and Riley [5] laid the foundations of the field. The modern anhedral can be traced back to the seminal work of Whitcomb [6] and Jacobs et al. [7] during the 1970s, which in turn lead to the KC-135 flight test program during the 1980s [8]. One of the more recent studies is that of Eppler, in 1997, who reviewed literature up to that time, and showed that a dihedral angle is more beneficial than anhedral [9]. A similar conclusion was drawn by industry during the development of what is now called the blended winglet [10] or the raked wingtip [11] although there are limited data in the public domain. In all of these designs, the main effect is on aerodynamics, and the target is always to

Received 10 December 2022; revision received 17 February 2023; accepted for publication 25 February 2023; published online 22 March 2023. Copyright © 2023 by the American Institute of Aeronautics and Astronautics, Inc. All rights reserved. All requests for copying and permission to reprint should be submitted to CCC at [www.copyright.com](http://www.copyright.com); employ the eISSN 1533-3868 to initiate your request. See also AIAA Rights and Permissions [www.aiaa.org/randp](http://www.aiaa.org/randp).

\*Graduate Research Assistant, Alfred Gessow Rotorcraft Center.

<sup>†</sup>Associate Professor, Alfred Gessow Rotorcraft Center.

<sup>‡</sup>Boeing Technical Fellow.

increase the effective span by minimizing induced drag. The induced drag benefit of the winglets is derived from the reduction in the strength of wingtip vortices that are also moved further away from the wing. A secondary benefit can be derived if a component of the winglet aerodynamic force can be pointed forward by suitable design. Many variants of winglets can be found today, variously named canted winglet, vortex diffuser, blended split, sharklet, spiroid winglet, tip sails, and others (see Ref. [12] for a review).

### B. Anhedral Tip in Helicopter Rotors

The effect of winglets on airplanes cannot simply be replicated on rotor blades. The  $g$ -loading at the tip is nearly 1000; hence structural pieces at the tip must have high strength and integrity, which normally means heavy weight. Moreover, the induced drag in rotors is due not only to the vortex at the individual tip but to vortices from all blades that collectively generate the inflow. The rapid variation of local flow, elastic motions, cyclic pitch, and vortex interactions make conditions at the rotor tip very different from wing tips. Nevertheless, the advent of modern composites has made the concept plausible, and some experiments have been carried out in the past. The earliest documented test was by Weller [13] at the NASA Langley Transonic Dynamics Tunnel, where performance and blade flap and lag moments were measured on a 1.37-m-radius four-bladed articulated rotor with a  $10^\circ$  anhedral tip from  $92\%R$ . Mantay and Yeager [14] carried out similar tests in the same tunnel on a 1.43-m-radius four-blade articulated rotor with the same anhedral tip but from  $95\%R$ . These two studies showed that rotor torque in hover and at advance ratios up to 0.4 was reduced at a given thrust level by the addition of anhedral.

Müller was the first to test winglets on rotor blades [15,16]. Two-bladed rotors of 0.545-m- and 0.48-m-radius were tested in hover and forward flight, respectively, with downward-pointing winglets. The winglet pushes the tip vortex down further away from the following blade. And a secondary vortex source at the bending point was observed as well [17]. Both effects of vortex structure result in higher rotor efficiency by reducing the induced velocities. Desopper et al. [18] tested a 0.857-m-radius three-bladed rotor with a swept tip with some anhedral at the ONERA S2 Chalais-Heudon wind tunnel. These tests during the 1980s and 1990s laid the foundation of modern anhedral tips on helicopter rotors. More recently, Huang et al. tested a 1-m-radius rotor for measuring acoustics [19]. Uluocak et al. tested a 0.65-m-radius rotor for measuring flowfield [20]. Most of these tests focused on performance.

None of the above tests included a dihedral–anhedral tip, which is a relatively newer concept. Boeing adopted the dihedral–anhedral tip for its Advanced Chinook Rotor Blades (ACRB) for the CH-47F, but there is no public domain information or data on these blades.

### C. Scope of Present Paper

To understand the behavior of dihedral–anhedral tips, test data from realistic rotor blades are vital. Good test data require systematic step-by-step investigation with clear documentation of not only data but also rotor properties. The model rotor should be Mach-scaled and representative of a modern blade, to allow measured to reflect actual flight, but at the same time be open-source, to allow peer review, and joint investigation by government, industry, and academia researchers. The present work is designed with these requirements in mind. The rotor geometry is inspired by the Boeing ACRB, but neither the geometry nor the properties bear any resemblance to the actual aircraft, so the model is generic. Following the introduction, Sec. II describes the overall technical approach. Section III describes the blades. Section IV describes the vacuum chamber tests and results. Section V describes the hover tests and results. The last section gives the conclusions.

## II. Technical Approach

A set of dihedral–anhedral tip composite blades are designed in consultation with Boeing to ensure that the geometry is realistic enough to be representative of a modern rotor and yet be open source. Three-dimensional blade models were built using Computer Aided Three-Dimensional Interactive Application software (CATIA),

meshed using Cubit, and analyzed using X3D. These models were used to guide the development of the design, and to perform pretest analysis to ensure structural integrity. Then the blades were fabricated and tested in-house—first in a 10-ft-diam vacuum chamber and then in a hover tower. A special-purpose hingeless hub was designed and fabricated in-house to excite the blades in the rotating frame in vacuum. The hover tests were carried out under steady and oscillatory loading conditions. The rotor properties and boundary conditions were measured and documented in detail for future analysts.

## III. Dihedral–Anhedral Tip Composite Blade

### A. Blade Design

The overall parameters of the rotor are shown in Table 1. The blade design is shown in Fig. 1. The rotor radius  $R$  is 0.853 m. The blade has a span of 0.7145 m placed at a root cut out of 0.1385 m ( $16.23\%R$ ). The chord is a uniform 0.08 m. The nominal rotational speed in revolutions per minute (RPM) is 2282, allowing the blade tip speed to reach 0.6 Mach number. There is a linear built-in twist of  $-16^\circ$  per span and an unsymmetric VR-7 airfoil (12% thickness-to-chord ratio), the definition of which can be found in Ref. [21]. As shown in Fig. 1, the blade has three main sections and two transition regions. The straight portion extends from the root cutout ( $16.4\%R$ ) to  $80\%R$  connecting to a  $5^\circ$  dihedral portion over  $80$ – $95\%R$ . The last portion is an anhedral of  $15^\circ$  over the last  $5\%R$ . Two transition regions were designed at the beginning of each dihedral/anhedral portion to ensure a smooth aerodynamic contour. Each transition region occupies the first  $0.5\%R$  of its portion. The dihedral/anhedral angles are defined using the quarter chord line with respect to the rotating plane. Moreover, the blade cross sections are rotated about the curved quarter chord line to form the built-in twist.

The blade has a uniform cross section, and there are two main structural members (Fig. 2). A D-spar is made of two layers of  $\pm 45^\circ$  IM7/8552 graphite/epoxy weave throughout the span, and the outer skin is made of one layer of the same composite material. The rest of the internal space is filled with Rohacell IG-31 foam separated into a fore core inside the D-spar and an aftcore. This general layout is similar to the blades reported recently in Refs. [22,23]. Successful testing reported therein was a factor in selection of the cross section. Leading-edge weights of 16 tungsten alloy rods are embedded in the fore foam core to bring the cross-sectional c.g. near the quarter chord while minimizing their effect on the blade structural stiffness. A 3.6-mm-long trailing edge tab is designed to obtain a better bond between the upper and lower skins at the trailing edge. The tip is deliberately designed to maintain the same cross section, so the only change is in the spanwise geometry, and this required a special construction. The special construction is described later in the section on fabrication.

### B. Fabrication and Instrumentation

A two-part blade mold was designed and manufactured (Fig. 3). Aluminum 5083 was selected as the material to limit the deformation due to the change in temperature.

The track and balance of the rotor depend on the similarity of the blades, and particular care must be taken for advanced geometry blades. To reduce dissimilarities, a strict fabrication procedure was followed (Fig. 4). Step 1 was the preparation of the internal components, including aluminum 7075 root insert and foam cores. The foam core was pressure molded for 90 minutes under a temperature of  $177^\circ\text{C}$  ( $350^\circ\text{F}$ ) to create the blade shape. The foam should be slightly larger than the blade contour to ensure a consistent core density.

**Table 1** Blade parameters

Parameter	English	Metric
Radius	33.6 in.	0.853 m
Chord	3.15 in.	0.08 m
Airfoil		VR-7
Twist		$-16^\circ$
Taper		Untapered
Normal tip Mach		0.6

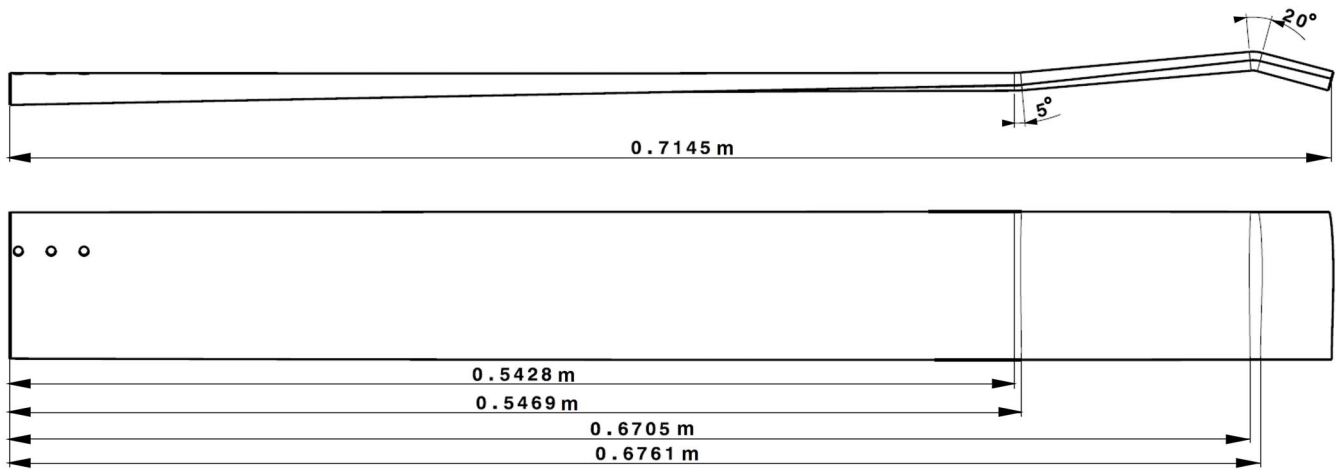


Fig. 1 Blade planform and tip geometry.

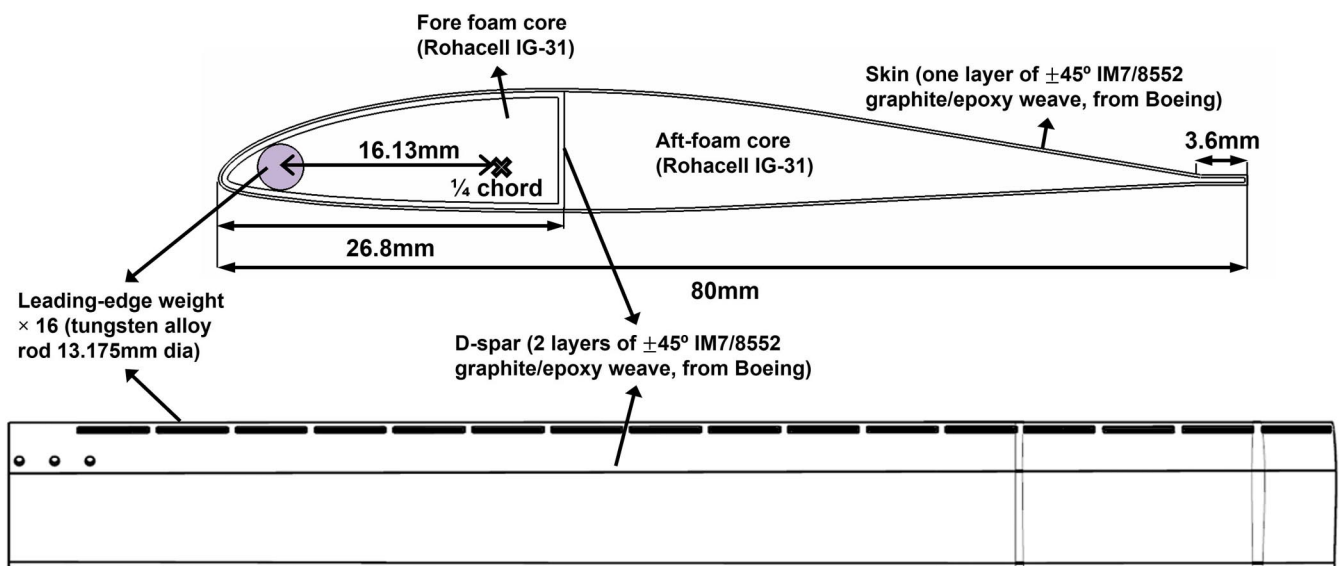


Fig. 2 Blade internal structure.

The separation of the fore and aftcores, as well as the milling of the slots for leading-edge weights were accomplished by a CNC machine. The core for the anhedral tip portions were made separately. The fore core with leading-edge weights and the root insert formed

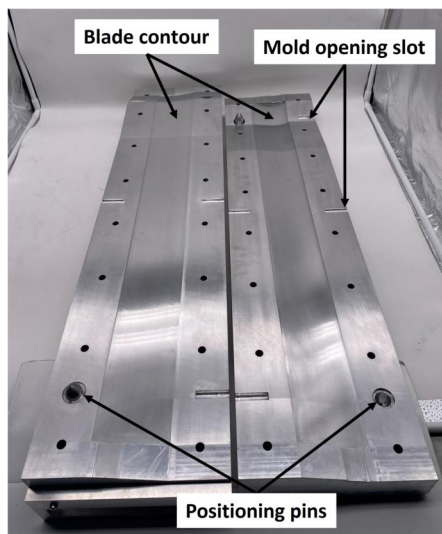


Fig. 3 Blade mold.

the D-spar mandrel. Step 2 was the assembly of the internal components. Both the D-spar mandrel and the aftcore were wrapped with a ply of film adhesive. As shown in Fig. 5, copper wires were embedded in the aftcore and pierced through the skin for instrumentation. The epoxy shown in Fig. 5 was for temporary protection for the wires. The blade surface was smoothed out in the end. Step 3 was the fabrication of the D-spar and Skin. The D-spar mandrel was wrapped with two plies of  $\pm 45^\circ$  IM7/8552 graphite/epoxy weave. The D-spar and aftcore assembly was wrapped by a ply of the same material, which is the blade skin. Step 4 was curing the blade. The uncured assembly was first protected by a ply of release film and then inserted into the mold. The cure cycle started at room temperature and held at  $177^\circ\text{C}$  ( $350^\circ\text{F}$ ) for 150 min. The tip geometry was formed by the pressure. No additional equipment was needed as curvature in the transition portions was small. The final step included trimming the resin extrusions and drilling the root insert holes. A total of six blades were fabricated. The weight of each component was measured in detail, and four blades with the most similarity were selected. The weight break-down of those blades is shown in Table 2. The root insert, fore core, leading-edge weight (LEW), and aftcore include the film adhesive.

All blades were instrumented to measure loads (Fig. 6). Three sets of full-bridge strain gauges measure flap bending, lag bending, and torsional moment at  $40\%R$ . A static loading frame was built to perform the calibration. The three sensors were calibrated together to account for structural coupling. The calibration resulted in a 3-by-3

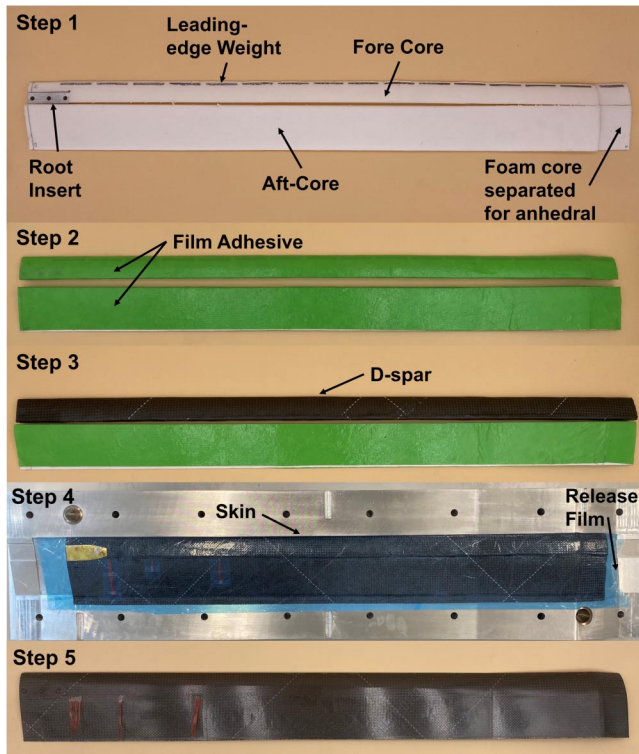


Fig. 4 Blade fabrication process.

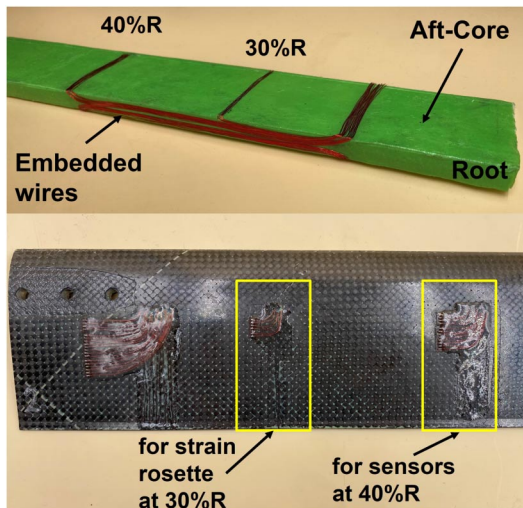
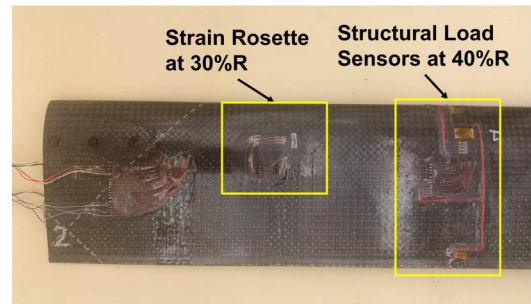


Fig. 5 Embedded wires for instrumentation.

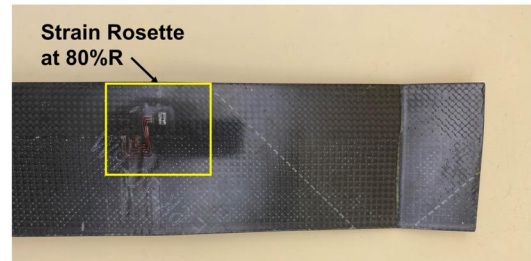
Table 2 Measured weight of each component in grams

Blade	Root insert	Fore core	LEW	Aftcore	Spar	Skin	Total
1	11.59	19.8	73.78	37.45	31.81	36.99	211.42
2	11.33	19.67	73.77	37.56	31.6	37.77	211.70
3	11.39	19.44	73.77	37.7	31.36	37.37	211.03
4	11.53	19.66	73.78	37.78	30.85	38.59	212.19

matrix for each blade that converted analog voltage to moment. During calibration, the flap bending moment was applied by force normal to the chord line at the blade root. Hence, the measured flap bending moment is referenced to the root chord line. Similarly, the lag bending moment is referenced to the root insert bolt hole axis, and the torsional moment is about the quarter chord line. This means that the structural loads were measured in the blade frame, which will rotate with the blade pitch input. As for surface strain, there are two



a) Instrumentation at root



b) Instrumentation at tip

Fig. 6 Blade instrumentation.

monitoring points: the top surface of 30%R near the root and the bottom surface of 80%R at the dihedral junction. Both the measurement points are on the quarter chord line. The surface strains were measured by strain rosettes, which allow the access of axial normal strain, chordwise normal strain, and in-plane shear strain. Finally, the four instrumented blades were ready for tests as shown in Fig. 7.

### C. Three-Dimensional Blade Structural Model

Three-dimensional finite element structural models were developed. The models were built directly from the computer-aided design (CAD) geometry in CATIA, solid-meshed in Cubit, and analyzed in X3D [24,25]. Although a full-fledged analysis is outside the scope of this paper, the models are documented to ensure completeness and consistency in property definition. The three main ingredients of the model were meshing with higher-order 27-noded hexahedral elements, chamber and hover boundary conditions, and composite material properties. The models are shown in Fig. 8. A straight blade of the same twist but without the dihedral-anhedral tip was also created. The aerodynamic and structural descriptions are identical except for the tip geometry. The two meshes have 32,398 and 40,602 nodes, respectively; hence the resolutions are comparable as well. The boundary condition is cantilevered at the root with a pitch bearing to allow pitch input.



Fig. 7 Final blades.

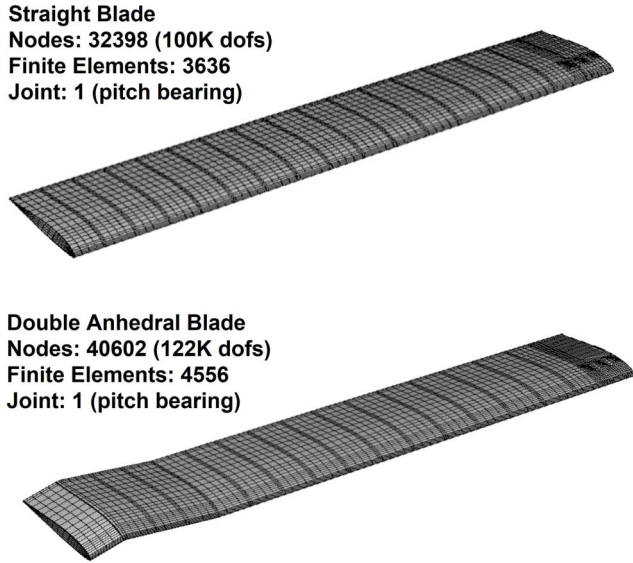


Fig. 8 Three dimensional mesh of blade models.

**D. Properties**

Based on the weight of each component measured during fabrication, the corresponding material densities were calculated using the volume extracted from the CAD geometry. These densities are listed in Table 3. The material elastic properties were refined based on in-house coupon testing [22]. The manufacturer (Hexcel)-supplied properties were  $E_1 = 85$  GPa,  $E_2 = 80$  GPa, and  $\mu_{12} = 0.131$ . All pretest analysis and prediction of rotating frequencies and strains were performed with the 3-D model. Although not needed for a 3-D analysis, cross-sectional stiffnesses were also measured to facilitate a one-dimensional beam analysis. The measured values are  $EI = 20$  N · m<sup>2</sup> in normal bending,  $EI = 937$  N · m<sup>2</sup> in chord bending, and  $GJ = 62$  N · m<sup>2</sup> in torsion. The predicted values from 3-D are  $EI = 24$  N · m<sup>2</sup> in normal bending,  $EI = 941$  N · m<sup>2</sup> in chord bending, and  $GJ = 76$  N · m<sup>2</sup> in torsion. More details can be found in Ref. [23]. The chordwise c.g. location was at quarter chord by design but measured to be between 28 and 29% of chord behind the quarter chord.

**IV. Vacuum Chamber Test**

Vacuum chamber tests were carried out to measure rotating natural frequencies and strains. Chamber tests are always performed to ensure structural integrity of a new rotor before hover tests, but with a special setup and actuation, frequencies and strains can be measured in the rotating frame. These data are crucial for proper validation of a rotor structural model.

**A. Chamber**

The vacuum chamber is typical—a 3.05-m-diam, 0.91-m-high cast iron cylindrical structure that can maintain up to 99% vacuum (Fig. 9). An electric motor is located outside and below the chamber that drives the rotor inside by a belt-pulley system through a vacuum-sealed bearing. The rotor can be spun up to 1400 RPM. A 65-channel slip

Table 3 Properties of each component

Component (material)	Density, kg/m <sup>3</sup>	$E_1$ , GPa	$E_2$ , GPa	$\mu_{12}$	$G_{12}$ , GPa
Skin, spar (IM7/8552 graphite-epoxy prepreg weave)	1,470	81.5	72.9	0.0755	5.45
Foam core (Rohacell IG-31)	190	0.036	—	0.3846	—
Leading-edge weight (tungsten)	15,287	650	—	0.2	—
Root insert (Al 7075)	2,750	68.9	—	0.33	—

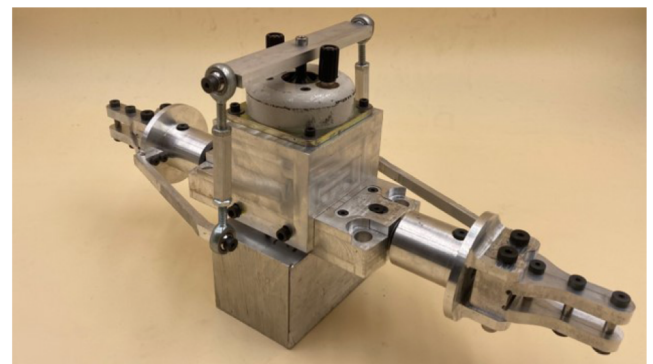


Fig. 9 Vacuum chamber.

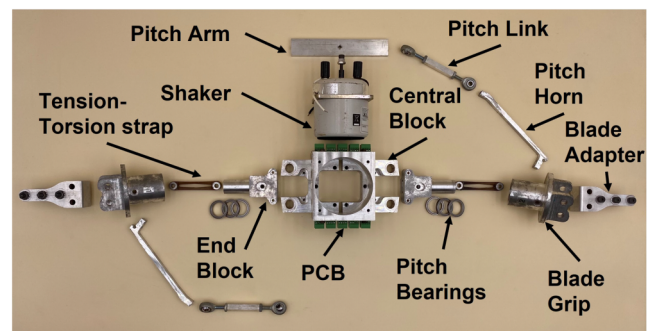
ring is connected to the rotor shaft, also below and outside the chamber, which is used to control the actuator on the rotor hub and communicate the sensor signal from the rotating to the fixed frame. The rotational speed is monitored by a gear-tooth wheel and an optical sensor. The actuator on the rotor hub is specially developed for this work.

**B. Hub Actuator**

A new two-bladed hingeless hub actuator was designed and fabricated in-house for the test. A two-bladed hub suffices for chamber tests because aerodynamics is irrelevant, and two blades are all that are needed to balance the centrifugal force. Figure 10a shows the assembled hub, while Fig. 10b shows the components. A hub central block is mounted on the shaft inside the vacuum chamber. The end



a) Chamber hub actuator



b) Components

Fig. 10 Vacuum chamber two-bladed hingeless hub and actuator.

blocks are held by the central block. The blade grip connects to the end block through a tension–torsion strap. The blade grip tube slips on the end block tube as a sleeve, with three pitch bearings in between two tubes. How the pieces fit together is shown in Fig. 11. A blade adapter is used to connect the blade to the hub. During the test, pitch motion is used to excite the blade, so a full pitch mechanism is built, including a pitch horn, pitch link, and a pitch arm to transform the linear motion of a shaker to the pitch motion at the blade grip. As only collective pitch input is needed, the input is applied in the rotating frame directly, so a swash plate is not necessary. The load path of this system is identified in Fig. 11. There are three main paths from the blade to the hub. The pitch moment is transferred via the pitch mechanism to the shaker. The tension–torsion strap takes the centrifugal force from the blade grip and passes it on to the end block. The strap is flexible in torsion to allow twist deformation induced by the pitch motion. Three pitch bearings on the end block tube carry the bending moments and shear forces. They also keep the outer tube and the inner tube aligned and separated to ensure each load has only one path.

Identifying the blade boundary conditions is important for analysis. Therefore, before the rotor is spun up, static load tests and nonrotating frequency tests were performed. From these, the stiffnesses in pitch (nose up), flap (vertical bending), and lag (in-plane bending, toward the trailing edge) were deduced. Note that a full 3-D model may not require these, but a beam model certainly will. They are also important for a physical understanding of the structure.

The setup for measuring the pitch stiffness is shown in Fig. 12. A static load was applied on the pitch link via a pulley and measured by a load cell. The deformation of the pitch horn was monitored by a laser sensor. Based on the pitch horn geometry and the pitch moment applied, the rotation about the pitch axis was determined, and from there, the pitch stiffness was calculated. To find the flap and lag root stiffnesses, another test was carried out, as shown in Fig. 13. These stiffnesses are hard to measure directly as they are an accumulated result of all the parts and pieces at the root end. So a combination of measurement and analysis was used. The hub actuator was used to excite a rectangular aluminum beam, and the beam response was recorded by the laser sensor. Taking the fast Fourier transform of the beam response, the nonrotating frequency was found. Then a structural model was built with a root spring, and the stiffnesses determined by tuning the model until predictions matched measurements.

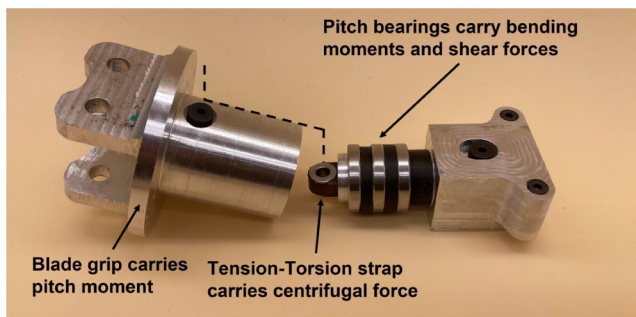


Fig. 11 Vacuum chamber hub bearing and load path.

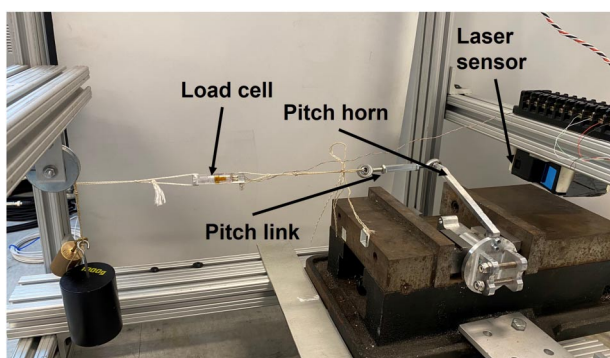


Fig. 12 Measurement of pitch stiffness.

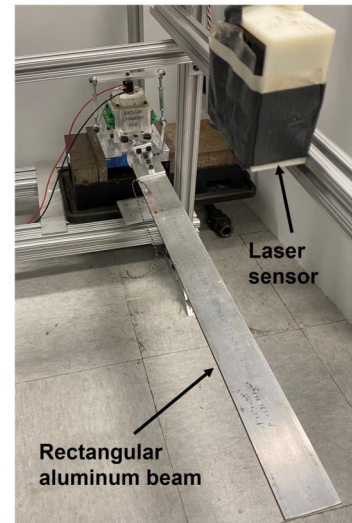


Fig. 13 Measurement of root flap and lag stiffnesses.

The elementary nature of the rectangular aluminum beam allowed verification with theoretical results. The final stiffnesses were 75, 900, and 900 N · m/rad for pitch, flap, and lag, respectively. The outer tube on the blade grip and the inner tube on the end block were the two components that affected the flap and lag stiffnesses the most. They have the same magnitude due to the circular cross section of the two components.

The final vacuum test setup is shown in Fig. 14. For the frequency test, the pressure inside the chamber was reduced to 99% vacuum (the maximum possible). Then the rotor RPM was adjusted by the motor controller. Once the RPM reached a target value, a frequency sweep was applied at the pitch input. The blade response was recorded via the strain gauge. This procedure was repeated for all rotor RPM, including at zero RPM to measure the nonrotating frequency (which matched with the static tests). For the strain test, the blade root pitch was fixed at 5.6 deg and an RPM sweep was carried out. The baseline case was recorded before spin-up. The strains were recorded for 3 s when the rotor speed stabilized at the desired RPM.

### C. Rotating Frequency

The blade strains to pitch frequency sweep were processed using fast Fourier transform to acquire the blade frequencies. Figure 15 shows an example of the frequency spectrum of a blade spinning at 200 RPM. The peaks at the multiples of the excitation voltage (60 Hz) were discarded. The remaining peaks were the rotating frequencies.

The measured fan plots are shown in Fig. 16. Predictions from the 3-D model (using X3D) are also shown for comparison. The triangles are measured frequencies; the different colors correspond to different blades. Three blades were tested. The solid lines are the predicted frequencies. The dashed lines are constant per-revolution values. Up to seven nonrotating frequencies and six rotating frequencies were captured. The predictions match well with the test data except for the highest mode. The crossover of the first two modes is also observed.

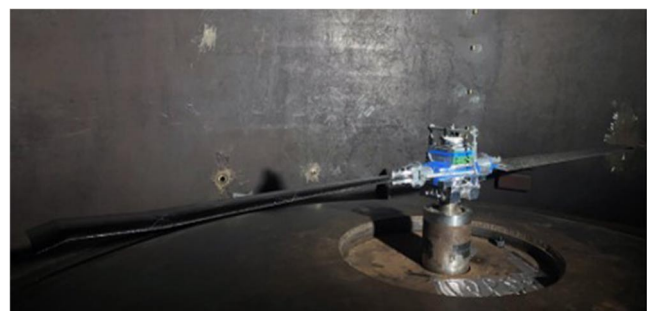


Fig. 14 Vacuum test setup.

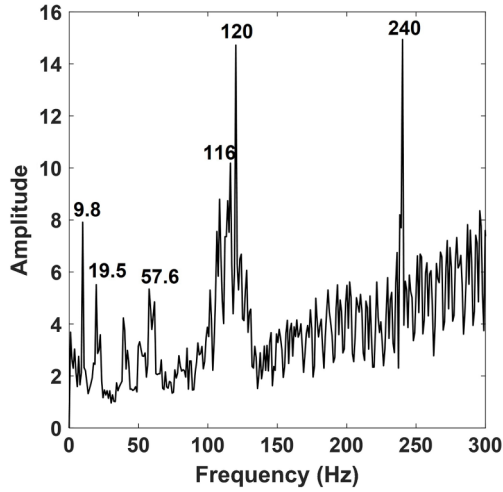


Fig. 15 Frequency spectrum of strain signal at 200 RPM.

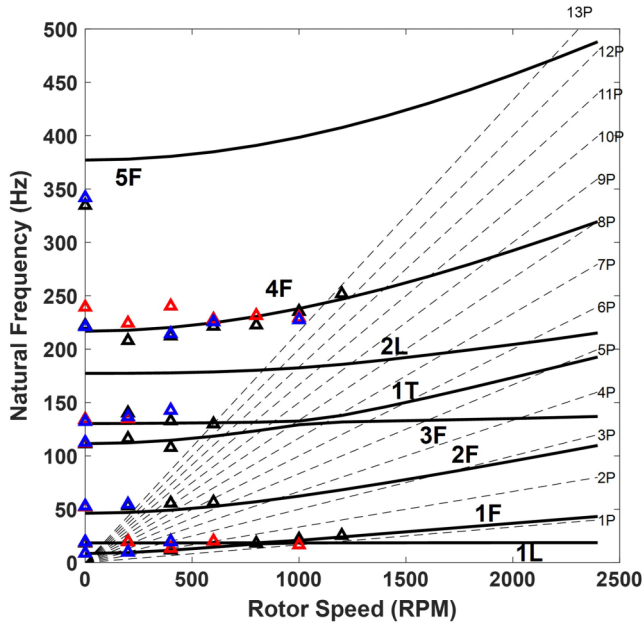


Fig. 16 Measured versus predicted fan plot of the dihedral-anhedral tip blade.

By analyzing the mode shape in X3D, each mode was identified. The modes are marked as F, L, and T, for flap, lag, and torsion, respectively. Due to the high lag stiffness, the test was unable to excite the second lag mode. This is the only mode missing from the data. The measured and predicted nonrotating frequencies are shown in Table 4 for further comparison.

With the 3-D structural model validated in terms of natural frequencies, the impact of the dihedral-anhedral tip could be analyzed by comparing it to the straight blade model. Figure 17 shows there are negligible differences in the first lag and the first three flap modes. The effect of the tip geometry starts to show from the first torsional mode and all higher modes thereafter. The local c.g. offset at the tip reduces the first torsional frequency, the second lag frequency,

Table 4 Measured and predicted nonrotating frequencies of the dihedral-anhedral tip blade

Parameter	1st flap	1st lag	2nd flap	3rd flap	1st torsion	2nd lag	4th flap	5th flap
Measurement, Hz	8.8	19.2	52.4	112.7	133.8	—	222.2	341.9
Prediction, Hz	8.5	18.3	46.2	114.2	130.3	—	216.8	377.2

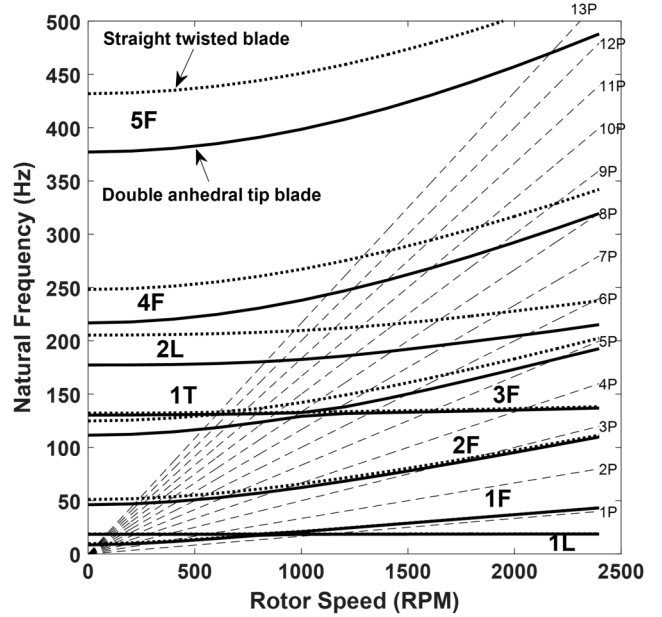


Fig. 17 Predicted fan plot of straight versus dihedral-anhedral tip blade.

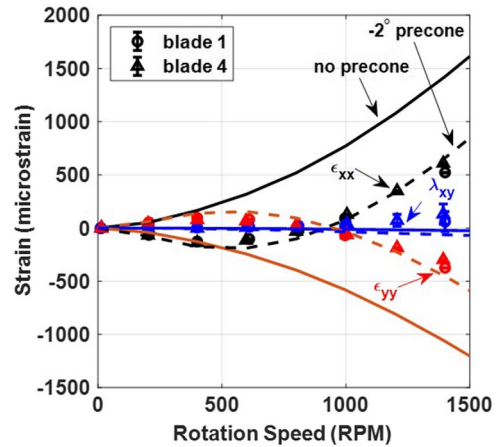


Fig. 18 Rotating strain at the top surface of 30% R.

and the fourth and fifth flap frequencies. In general, it appears to make the blade softer.

#### D. Rotating Strains

The measured strains at the top surface at 30%R are shown in Fig. 18. Axial  $\epsilon_{xx}$ , chordwise  $\epsilon_{yy}$ , and in-plane shear  $\gamma_{xy}$  strains were measured. Measurements from two blades (markers) show generally good repeatability. The X3D prediction is overlaid (solid and dashed lines). The solid lines are from the baseline model. Examination of the discrepancies revealed that the vacuum chamber hub had in fact a  $-2^\circ$  precone angle at the end block (a built-in flap down angle). When this precone angle was included in the model, the agreement between test data and prediction became satisfactory. The dash line shows the prediction with precone. Thus, the 3-D strain validation allowed the capture of unintended geometric imperfections that can be missed by frequencies but nevertheless are important for stresses/strains.

#### V. Hover Test

The hover stand is shown in Fig. 19 and the overall parameters are summarized in Table 5. The rotor solidity is 0.1 with a root cutout of 16.2%R. The hover hub is stiffer than the vacuum chamber and can be considered rigid. The rotor frequencies predicted with rigid boundary conditions are shown in Fig. 20. The vertical lines show the test



Fig. 19 Hover test stand.

Table 5 Rotor parameters

Parameter	Value
Number of blades	4
Hub type	Hingeless
Radius	0.853 m
Root cutout	16.2%R
Solidity	0.1
Pitch horn chordwise offset	0.03 m
Pitch link radial location	7%R
Pitch link cross section	Square 9.6 mm × 9.6 mm
Pitch horn and link rotational stiffness	5675 N · m <sup>2</sup> /rad
RPM nominal	2282
RPM test	1000, 1522, 1902, 2282
$M_{tip}$ test	0.26, 0.4, 0.5, 0.6

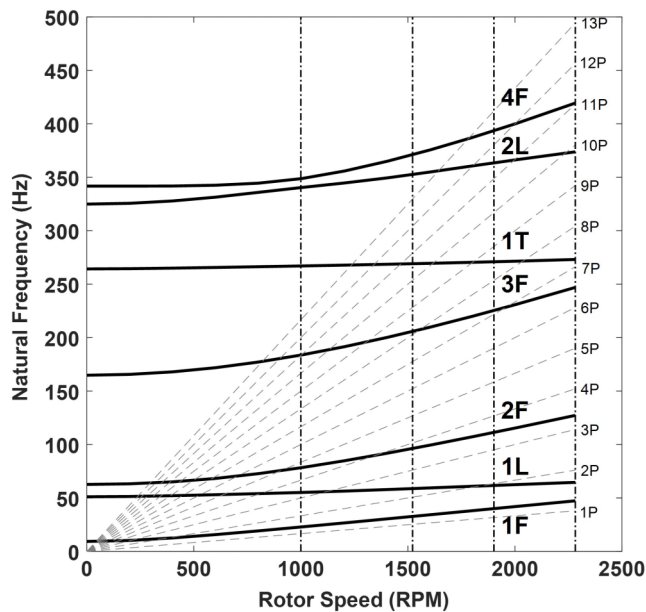


Fig. 20 Fan plot of the hingeless rotor.

RPMs. These were selected for distinct tip Mach numbers  $M_{tip}$ . The 0.2 and 0.3 values were avoided for resonance crossings. The first lag mode had an additional resonance crossing near 1902 RPM, but during the test, the resonance was observed to occur earlier and died quickly as the RPM passed through.

Figure 21 shows the main components of the hover stand. The rotor was driven by a hydraulic motor and a belt-pulley system. A five-component balance was installed in the fixed frame to measure the hub loads, while the rotor torque was measured in the rotating frame by a torque sensor on the shaft. The rotational speed and the rotor azimuth angle were monitored by an optical sensor and a shaft encoder, respectively. Besides the blade structural loads and

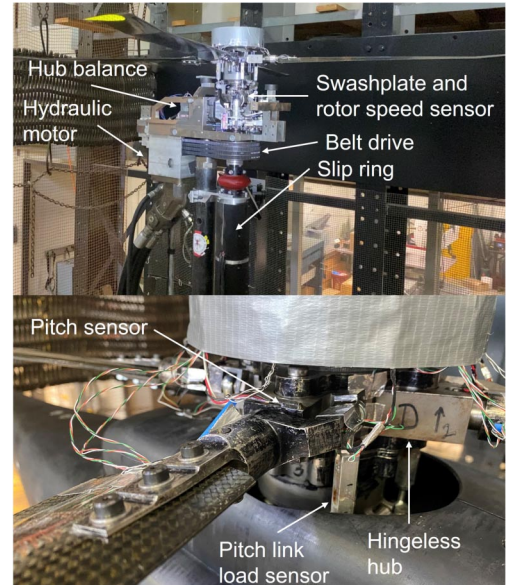


Fig. 21 Hingeless rotor test setup on the hover tower.

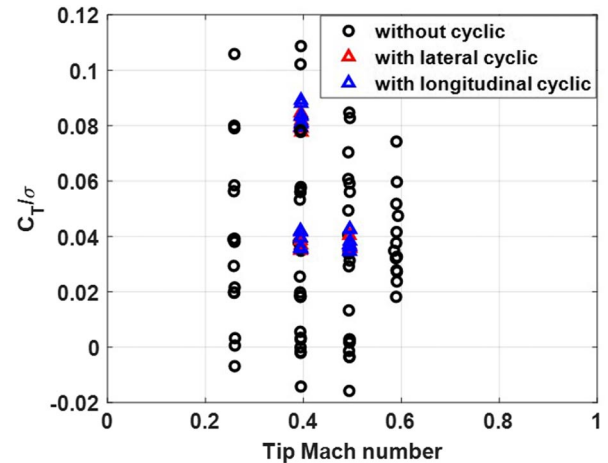


Fig. 22 Hover test envelope:  $C_T/\sigma$  versus  $M_{Tip}$ .

surface strains, blade pitch angles and pitch link loads were also measured.

The test envelope in terms of tip Mach number and blade loading is shown in Fig. 22. There are 80 test points of steady hover (collective input only) and 39 test points of unsteady hover (with cyclic inputs to induce dynamic loading). The test began by setting the rotor speed first, then collective, and finally cyclic. The rotor was balanced and tracked at each RPM to ensure blade-to-blade similarity.

#### A. Collective Sweeps

At each RPM the rotor collective is swept. The collective is defined as the pitch at the 75% of span  $\theta_{75}$ , so the total pitch angle at any section at radial station  $r$  is the collective added to the twist:  $\theta(r) = -16^\circ(r/R - 0.75) + \theta_{75}$ . The rotor hover performance is shown in terms of power ( $C_P/\sigma$ ) and figure of merit versus blade loading ( $C_T/\sigma$ ) in Figs. 23 and 24, respectively. The figure of merit is ideal power divided by the actual power:  $FM = C_T^{3/2}/\sqrt{2}C_P = 0.707C_T^{3/2}/C_P$ . The data collapse to similar values except at the lowest tip Mach number. This is due to the low-Reynolds-number effects. No stall is observed. The maximum figure of merit attained is 0.713, which occurs at a blade loading of 0.113.

The blade structural loads measured at 40%R are shown in Figs. 25 and 26. The different marker symbols represent different blades. Positive flap and lag bending moments indicate bending up and aft, respectively. The flap moment increases with collective but decreases

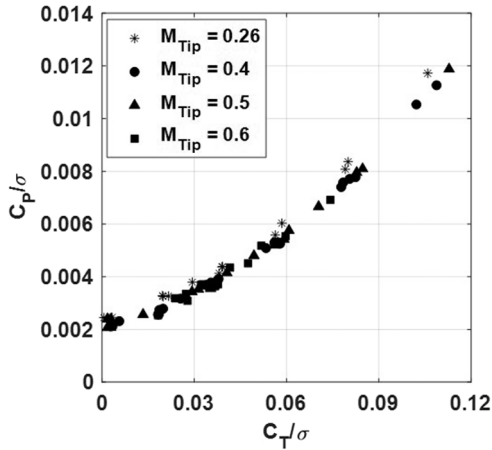


Fig. 23 Hover  $C_p/\sigma$  versus  $C_T/\sigma$ .

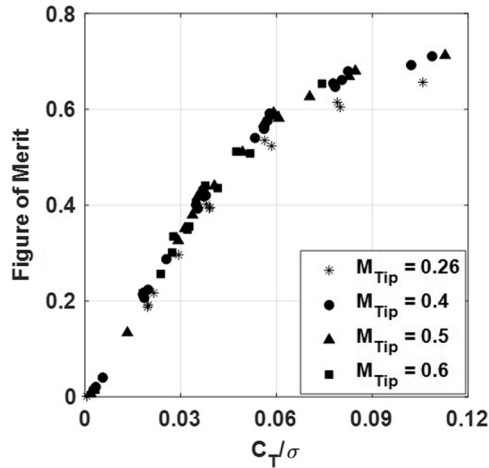


Fig. 24 Figure of merit versus  $C_T/\sigma$ .

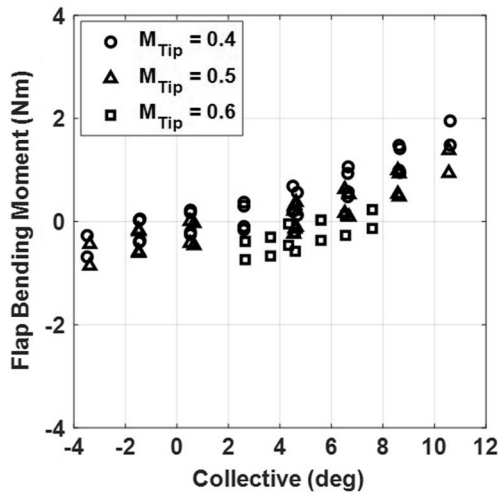


Fig. 25 Flap bending moment at 40%  $R$ .

with tip Mach number. The former is due to the obvious increase in lift. The latter is due to increases in the centrifugal force, which generates a bending down moment. The out-of-plane c.g. offset due to the tip adds to this effect. The lag bending shows no change with collective, but increases with tip Mach number. This is likely due to the increase in compressibility drag. The pitch link loads are nose down (so the link is in compression), typical of all rotors, as shown in Fig. 27. The pitch link loads grow with both collective and tip Mach number. The effect of the latter is quite dramatic.

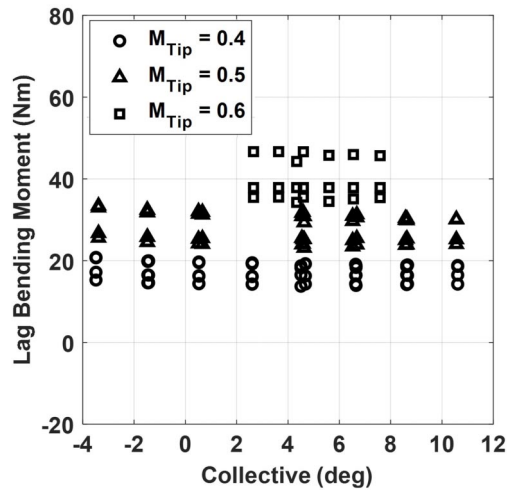


Fig. 26 Lag bending moment at 40%  $R$ .

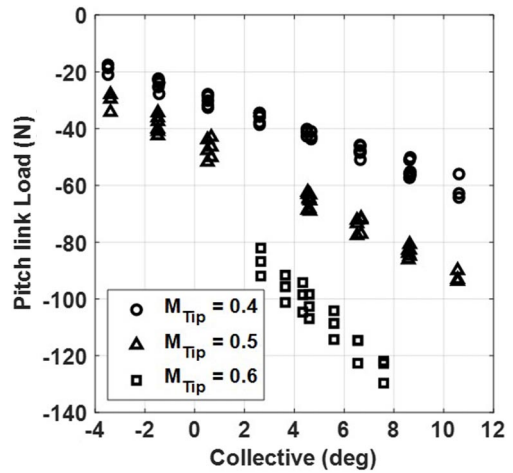


Fig. 27 Pitch link load.

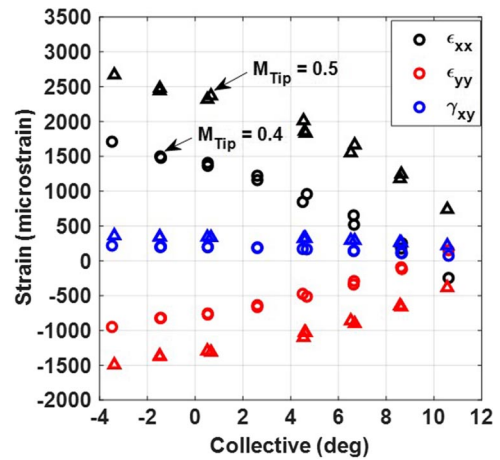


Fig. 28 Strains on the top surface at 30%  $R$ .

Strains measured on the top surface at 30%  $R$  reveal a clear pattern (Fig. 28). The axial strain  $\epsilon_{xx}$  decreases as the collective angle increases. The extension generated by the centrifugal force is countered by the compression generated by the lift. As the tip Mach number increases, the growth of centrifugal force outweighs that of the lift. Therefore, the axial strain increases. The chordwise strain behaves in the opposite fashion to that of the axial strain based on the local Poisson's ratio. The in-plane shear strain  $\gamma_{xy}$  always remains low. Compared to the strain near the root, strains measured on the bottom surface at 80%  $R$ —close to the dihedral junction—is much lower (Fig. 29). The data are also

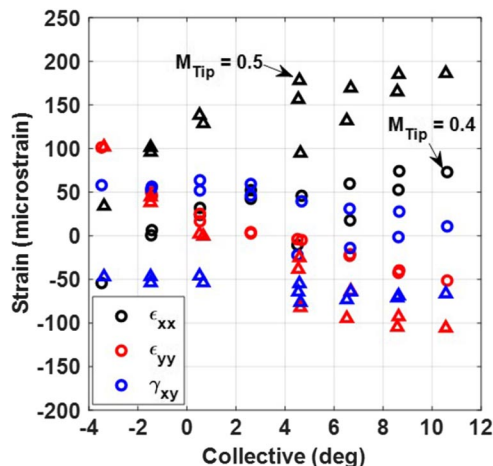


Fig. 29 Strains on the bottom surface at 80%  $R$ .

more scattered due to the low magnitude. However, there are trends that can be identified. The axial strain increases as the collective angle increases. Both centrifugal force and the lift generate extension at this location, which grow with the rotor speed. The magnitude of the in-plane shear is comparable to the normal strains.

### B. Cyclic Sweeps

In contrast to steady hover, cyclic inputs induce dynamic hub moments and blade loads and strains. The cyclic inputs can be cosine (lateral) and sine (longitudinal) inputs, so the pitch angle at any section at radial station  $r$  is now  $\theta(r) = -16^\circ(r/R - 0.75) + \theta_{75} + \theta_{1C} \cos \psi + \theta_{1S} \sin \psi$ , where the angle  $\psi$  is the blade azimuth;  $\psi = 0^\circ$  when a blade passes over the tail line.

Figure 30 shows the hub rolling and pitching moments for a lateral cyclic ( $\theta_{1C}$ ) sweep at two collective ( $\theta_{75}$ ) settings. Even though hover is symmetric for the rotor, the rolling moment is defined positive starboard, and the pitch moment positive nose-up relative to the fuselage shown in Fig. 19. The moments show a linear relationship with the lateral cyclic control, as expected. The rolling moment increases with collective; however, the pitching moment remains unchanged. The magnitudes of the rolling and pitching moments are comparable. This indicates that the phase angle between the control input and the blade response is close to  $45^\circ$ , which corresponds to the high flap frequency of 1.27/rev (meaning  $1.27 \times$  rotor speed  $\Omega$ ) of this hingeless rotor. The hub moments for a longitudinal cyclic ( $\theta_{1S}$ ) sweep are shown in Fig. 31. Similar observations can be made, except now the pitching moment is sensitive to collective instead of the rolling moment. It can be seen that there are nonzero pitching moment when there is no lateral or longitudinal cyclic input.

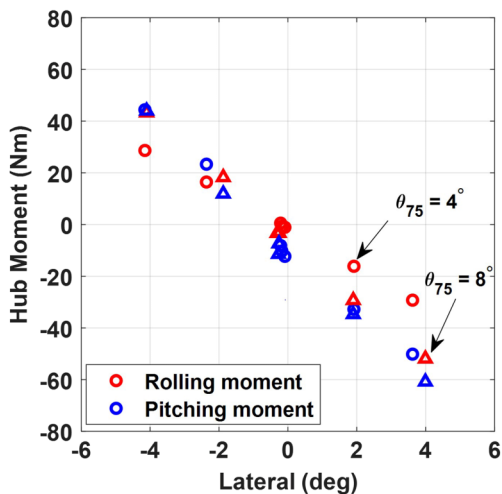


Fig. 30 Hub moment versus lateral cyclic ( $M_{\text{Tip}} = 0.4$ ).

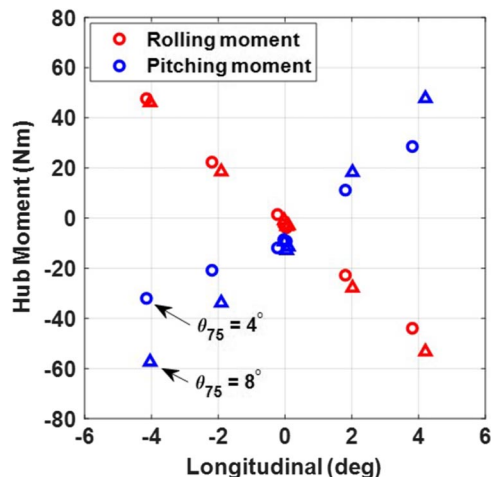


Fig. 31 Hub moment versus longitudinal cyclic ( $M_{\text{Tip}} = 0.4$ ).

The source of this discrepancy is unclear, but likely a measurement error due to cross-coupling of thrust and pitching moment channels.

A large number of dynamic cases were recorded in the test. Two interesting cases with collective angles of  $4^\circ$  ( $C_T/\sigma = 0.04$ ) and  $8^\circ$  ( $C_T/\sigma = 0.084$ ) are examined here. Both are at a tip Mach number of 0.4 and with lateral cyclic input of  $4^\circ$ . Blade loads and pitch link load are shown in Figs. 32–34. The lines show measurements from different

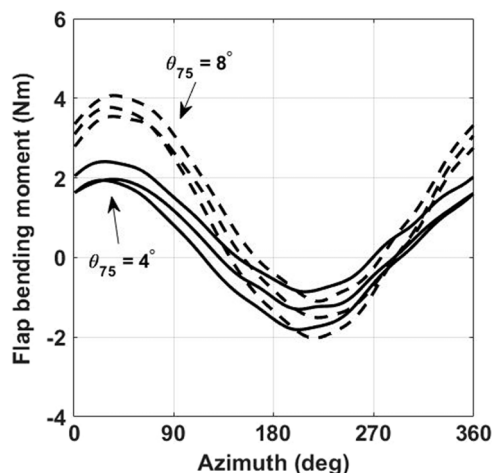


Fig. 32 Flap bending moment at 40%  $R$  versus azimuth ( $M_{\text{Tip}} = 0.4$ ,  $\theta_{1C} = 4^\circ$ ,  $C_T/\sigma = 0.04$ , and  $0.084$ ).

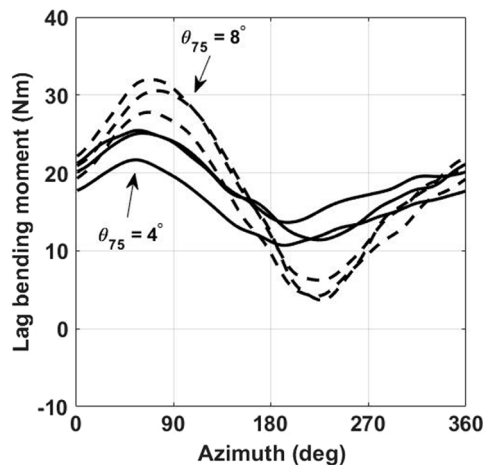


Fig. 33 Lag bending moment at 40%  $R$  versus azimuth ( $M_{\text{Tip}} = 0.4$ ,  $\theta_{1C} = 4^\circ$ ,  $C_T/\sigma = 0.04$ , and  $0.084$ ).

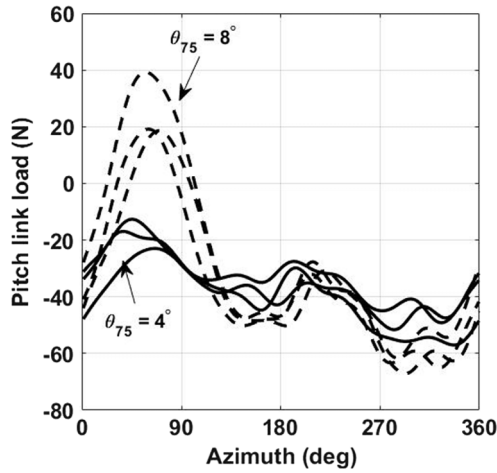
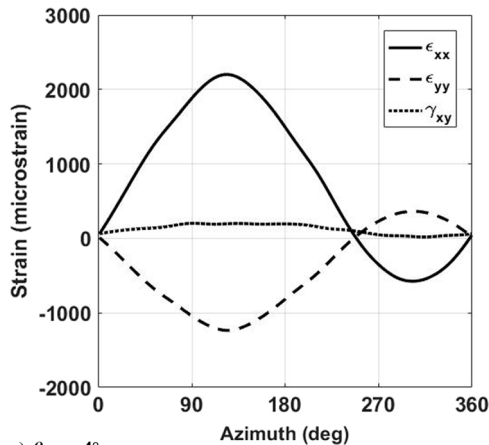
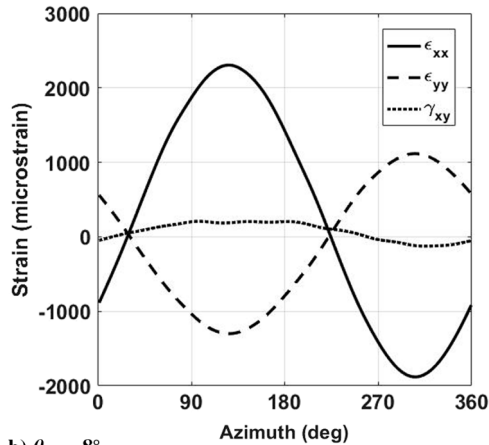


Fig. 34 Pitch link load versus azimuth ( $M_{Tip} = 0.4$ ,  $\theta_{1C} = 4^\circ$ ,  $C_T/\sigma = 0.04$ , and  $0.084$ ).

blades. Ideally, they should be identical, but in practice they reveal the extent of blade-to-blade dissimilarity. The blade flaps up in the first quadrant of the disk, which is consistent with the hub moments. The loading is dominated by a 1/rev component (1/rev = once per revolution; same as rotor speed  $\Omega$ ). The lag bending moment behaves similarly to flap but are an order of magnitude higher. The peak-to-peak magnitudes increase with the collective angle. The higher harmonics are most pronounced in the pitch link load with the higher collective showing a high impulse in the first quadrant. The dominant higher harmonic component in pitch link load is the 2/rev component.

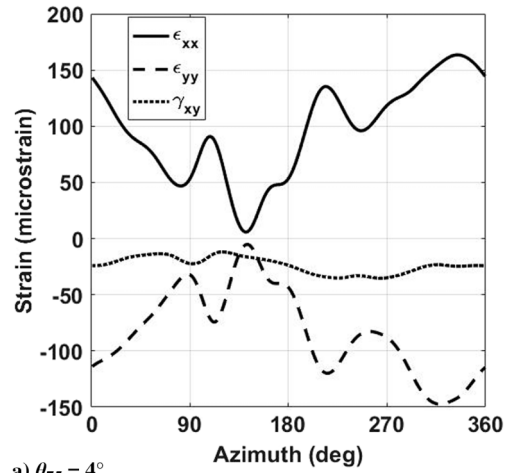


a)  $\theta_{75} = 4^\circ$

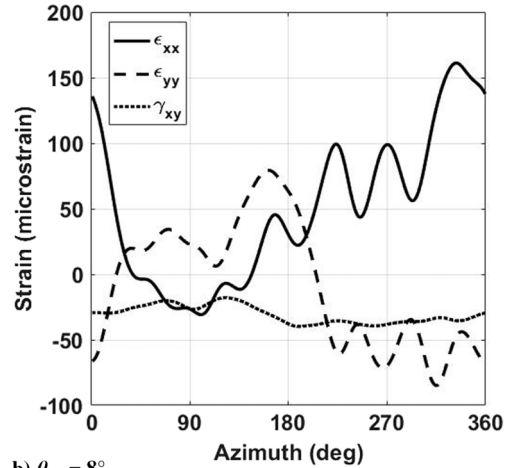


b)  $\theta_{75} = 8^\circ$

Fig. 35 Strain on the top surface of 30%R ( $M_{Tip} = 0.4$ ,  $\theta_{1C} = 4^\circ$ ,  $C_T/\sigma = 0.04$ , and  $0.084$ ).



a)  $\theta_{75} = 4^\circ$



b)  $\theta_{75} = 8^\circ$

Fig. 36 Strain on the bottom surface of 80%R ( $M_{Tip} = 0.4$ ,  $\theta_{1C} = 4^\circ$ ,  $C_T/\sigma = 0.04$ , and  $0.084$ ).

During the impulse the loads change from compression (negative) to extension (positive). The reasons are not apparent but perhaps related to local transonic flow near the blade tip driving impulsive pitching moments. Thus the data set likely contains enough variety to challenge high-fidelity analysis tools.

The dynamic surface strains are shown in Figs. 35 and 36. High-fidelity 3-D models would benefit from these strains. The strain on the top surface at 30%R has a strong 1/rev component and follows the flap bending moment. The highest axial strain occurs in the second quarter of the disk. As the collective increases, the magnitude of the valley grows significantly. The in-plane shear remains comparatively low. On the bottom surface at 80%R, the strains are far more interesting as anticipated. Recall that this is the location where the dihedral beings. Significant higher harmonics are observed over and above the baseline 1/rev component. The source of these harmonics is not clear; high-fidelity analysis is expected to shed light on these in future. The pattern changes with increase in collective, which more harmonics being introduced. How much of this behavior is due to the dihedral-anhedral tip is unknown and needs to be identified through analysis, but the behavior is quite atypical of straight blades.

## VI. Conclusions

Experimental investigations were performed on a Mach-scaled dihedral-anhedral tip composite rotor of 0.853 m (2.8 ft) radius. Hover tests were carried out under steady and oscillatory loading conditions. Rotating frequencies, strains, performance, blade loads, and pitch-link load were measured. A special-purpose hub actuator was developed to measure rotating frequencies in a vacuum chamber. Geometry and properties were thoroughly documented to aid future

analysts. Three-dimensional finite element models were developed to verify completeness and consistency of properties and data. Based on this work, the following conclusions were drawn.

1) The rotating blade natural frequencies can be measured accurately in a vacuum chamber with high-frequency pitch actuation. In the present work, up to seven modes could be excited. Predictions from a 3-D finite element model showed good agreement with the measurements and revealed the character of these modes. A high frequency lag mode that was predicted by the analysis could not be captured by the experiment.

2) The dihedral-anhedral tip seems to affect the first torsion mode and thereafter all higher modes. The local c.g. offset at the tip in the vertical direction generally lowers the blade frequencies and makes the blade richer in harmonic content.

3) The rotating strains predicted by the 3-D model generally correlated well with the test data. The impact of imperfections in the hub, such as an inadvertent precone angle, could be inferred from the surface strains, and predicted successfully after proper corrections to the geometry inputs. This conclusion also showed the importance of analysis in reporting test data.

4) During hover test, the maximum figure of merit reached 0.71 at a blade loading of around 0.1. The effect of tip Mach number was insignificant between 0.4 and 0.6. At 0.26 some deterioration was seen likely due to low-Reynolds-number effect on sectional drag. Thus future analysts should include appropriate fidelity or corrections.

5) A vertical c.g. offset at the tip has subtle but significant effects on blade loads. A reduction in flap bending moment is expected due to the additional downward moment generated by an upward vertical offset and vice versa. The present blades have a slight upward offset. This effect is found consistently with change in collective (lift) and tip speed (centrifugal force).

6) Pitch link loads showed a high compression-extension impulse in the first quadrant. This impulse was quite pronounced at a higher collective.

7) Interesting higher-harmonic strain patterns were observed at the junction between the main and dihedral portion of the blade at 80%R. The strain patterns inboard at 30%R followed a simpler 1/rev behavior although the oscillatory magnitudes were an order of magnitude higher.

In summary, the present measurements would offer an interesting validation test case for advanced comprehensive rotor analysis. Future research will carry out such analysis and conduct testing in forward flight at the Glenn L. Martin wind tunnel. It will also include a baseline straight blade for a consistent test to test comparison.

### Acknowledgments

This work was supported by Boeing with technical and programmatic oversight from Senior Technical Fellow Daniel Newman. Additional support was obtained from the U.S. Army/Navy/NASA Vertical Lift Research Center of Excellence VLRCE grant W911W611 20012, with technical monitoring from Mahendra Bhagwat.

### References

- [1] Lanchester, F. W., "Improvements in and Relating to Aerial Machines," British Patent No. 3608, Feb. 1898, pp. 1–8.
- [2] Reid, E. G., "The Effects of Shielding the Tips of Airfoils," NACA TR 201, 1924.
- [3] Hemke, P. E., "Drag of Wings with End Plates," NACA TR-267, Jan. 1928.
- [4] Mangler, W., "The Lift Distribution of Wings with End Plates," NACA TM-856, April 1938.
- [5] Riley, D. R., "Wind-Tunnel Investigation and Analysis of the Effects of End Plates on the Aerodynamic Characteristics of an Unswept Wing," NASA TN-2440, Aug. 1951.
- [6] Whitcomb, R. T., "A Design Approach and Selected Wind Tunnel Results at High Subsonic Speeds for Wing-Tip Mounted Winglets," NASA TN D-8260, July 1976.
- [7] Jacobs, P. F., Flechner, S. G., and Montoya, L. C., "Effect of Winglets on a First-Generation Jet Transport Wing," NASA TN D-8473, June 1977.
- [8] Barber, M. R., and Selegan, D., "KC-135 Winglet Program Review," NASA CP-2211, Jan. 1982.
- [9] Eppler, R., "Induced Drag and Winglets," *Aerospace Science and Technology*, Vol. 1, No. 1, Jan. 1997, pp. 3–15. [https://doi.org/10.1016/S1270-9638\(97\)90019-5](https://doi.org/10.1016/S1270-9638(97)90019-5)
- [10] Faye, R., Laprete, R., and Winter, M., "Blended Winglets," *Aero Magazine*, Boeing, No. 17, Jan. 2002.
- [11] Herrick, L. L., Bays-Muchmore, C. B., Hoffman, M. S., LeGrand, L., Ogg, S. S., Paul, B. P., Visser, K. D., and Wells, S. L., "Blunt-Leading-Edge Raked Wingtips," US Patent No. 6089502, July 2000.
- [12] Guerrero, J. E., Wittkowski, K., and Sanguineti, M., "Variable Cant Single Winglets for Improvement of Aircraft Flight Performance," *Meccanica*, Vol. 55, No. 10, Oct. 2020, pp. 1917–1947. <https://doi.org/10.1007/s11012-020-01230-1>
- [13] Weller, W. H., "Experimental Investigation of Effects of Blade Tip Geometry on Loads and Performance for an Articulated Rotor System," NASA TP-1303, AVRADCOM TR 78-53, 1979.
- [14] Mantay, W. R., and Yeager, W. T., "Parametric Tip Effects for Comformable Rotor Applications," NASA TM-85682, Aug. 1983.
- [15] Müller, R. H. G., "The Influence of Winglets on Rotor Aerodynamics," *12th European Rotorcraft Forum*, Garmisch-Partenkirchen, Germany, 1986; also *Vertica*, Vol. 11, No. 4, 1987.
- [16] Müller, R. H. G., "Winglets on Rotorblades in Forward Flight—A Theoretical and Experimental Investigation," *14th European Rotorcraft Forum*, Milano, Italy, 1988; also *Vertica*, Vol. 14, No. 1, 1990.
- [17] Müller, R., "Special Vortices at a Helicopter Rotor Blade," *Journal of the American Helicopter Society*, Vol. 35, No. 4, Oct. 1990, pp. 16–22. <https://doi.org/10.4050/JAHS.35.16>
- [18] Desopper, A., Lafon, P., Philippe, J. J., and Prieur, J., "Effect of an Anhedral Sweptback Tip on the Performance of a Helicopter Rotor," *Vertica*, Vol. 12, No. 3, 1988, pp. 345–355.
- [19] Huang, S., Fan, F., Yuan, M., and Sun, W., "Aerodynamic Performance and Aeroacoustic Characteristics of Model Rotor with Anhedral Blade Tip in Hover," *Transactions of Nanjing University of Aeronautics and Astronautics*, Vol. 35, No. 1, March 2018, pp. 162–169. <https://doi.org/10.16356/j.1005-1120.2018.01.162>
- [20] Uluocak, S., Perçin, M., and Uzol, O., "Experimental Investigation of Tip Anhedral Effects on the Aerodynamics of a Model Helicopter Rotor in Hover," *Aerospace Science and Technology*, Vol. 113, June 2021, pp. 1–15. <https://doi.org/10.1016/j.ast.2021.106671>
- [21] Dadone, L., "U.S. Army Helicopter Design Datcom Volume I—Airfoils," USAAMRLD CR 76-2, Sept. 1976.
- [22] Chi, C., Datta, A., Chopra, I., and Chen, R., "Three-Dimensional Strains on Twisted and Swept Composite Rotor Blades in Vacuum," *Journal of Aircraft*, Vol. 58, No. 1, Jan. 2021, pp. 1–16. <https://doi.org/10.2514/1.C035746>
- [23] Sutherland, J., and Datta, A., "Fabrication, Testing, and 3-D Comprehensive Analysis of Swept Tip Tiltrotor Blades," *Journal of the American Helicopter Society*, Vol. 68, No. 1, Jan. 2023, pp. 1–17. <https://doi.org/10.4050/JAHS.68.012002>
- [24] Staruk, W., and Datta, A., "Gimballed Tiltrotor Conversion Flight Loads Prediction Using 3-D Structural Analysis," *Journal of Aircraft*, Vol. 56, No. 2, March–April 2019, pp. 758–770. <https://doi.org/10.2514/1.C035075>
- [25] Patil, M., and Datta, A., "A Scalable Time-Parallel Solution of Periodic Rotor Dynamics in X3D," *Journal of the American Helicopter Society*, Vol. 66, No. 4, Oct. 2021, pp. 1–16. <https://doi.org/10.4050/JAHS.66.042007>